Full–length paper

Bandgap mapping for III–V quantum well by electron spectroscopy imaging

Jin-Sheng Tsai[1], Ji-Jung Kai[1], Li Chang[2] and Fu-Rong Chen[1,*]

[1]Department of Engineering and System Science, National Tsing Hua University and [2]Department of Materials Science and Engineering, National Chiao-Tung University, Hsin Chu, Taiwan, Republic of China
*To whom correspondence should be addressed. E-mail: frchen@ess.nthu.edu.tw

Abstract

The concept of 'bandgap mapping' was proposed originally to map the inhomogeneity of band energy in III–V semiconductors with a spatial resolution of a few nanometres in a scanning transmission electron microscope with the focus beam mode. In this paper, several techniques were developed to demonstrate the possibility to map the distribution of bandgap energies for GaN/AlN quantum-well structures using electron spectroscopy imaging (ESI). The phase correlation function was used to register different energy-loss images among ESI series with an accuracy of 1 pixel. The energy dispersion of ESI series was improved by a fast Fourier transform interpolation method. An iterative multivariable least square algorithm was derived to refine the fitting of the single scattering distribution to an analytic form of the density of states function $a(E - E_g)^{0.5}$. The inhomogeneity of the band energy of the quantum well can be revealed from the band-energy map. A threshold filter method is applied to estimate the average value and SD of the bandgap energy from barrier and well regions in the energy map. The average bandgap energy of AlN and GaN is determined to be 5.62 ± 0.35 and 3.87 ± 0.36 eV, respectively. The effect of delocalization on the accuracy of band-energy determination is discussed. The $2\sigma_{E_g}$ accuracy of this analysis is comparable to half of the energy resolution of the ESI experiment.

Keywords bandgap mapping, band energy, electron spectroscopy imaging, III–V quantum well

Received 17 December 2003, accepted 21 June 2004

Introduction

Gallium nitride (GaN) and its alloys with In and Al are used widely in device applications such as light-emitting diodes and lasers where the wavelength can, in principle, be varied from the red to the ultraviolet region [1,2]. Although GaN-based optoelectronic devices have already been commercialized with great success, understanding and controlling the optical–dielectric properties and the energy bandgap of devices remains important for device qualities and processing. Although optical techniques have higher energy resolution (~2 meV as compared with ~300 meV) for bandgap measurements, they are restricted to spatial resolution at the submicron level for transmission measurements and only direct transitions across the bandgap can be studied [3]. For an experimental approach to the understanding of local optical properties, spatially resolved methods at the

nanometre level are necessary. In recent years, several studies of the optical properties and energy bandgap of GaN and related materials, such as InGaN and AlN, using electron energy-loss spectroscopy (EELS) have been reported [4–10]. Basically, in the low-loss region ($<\sim50$ eV), the EELS spectrum measures an energy-loss function that depends on the joint density of states $\rho(E)$ for transitions between the valence and conduction band weighted by the matrix element $M(E) = \Sigma_{i,f}|<f|\boldsymbol{q}\cdot\boldsymbol{r}|i>|^2$ of the individual transitions, where $|i>$ and $|f>$ represent the initial and final states of transition, respectively, and $\boldsymbol{q}$ is the momentum transfer [11]. In the low-loss regime, the initial state is the valence state. The collective excitation effects are also important in the low-loss regime. In contrast to the ionization edges where the initial state is a core state with a narrow range, the valence states have a broad energy range, such

that a joint density of states (DOS), $\rho(E)$, is related to a convolution of occupied and unoccupied states.

After proper removal of the zero-loss peak and deconvolution of the plural scattering effect, the single scattering distribution (SSD), $S(E)$, and the product $M^2\rho$ can be obtained with the same energy-dependence [3]. In the dielectric formulation, the SSD can be described as the response of the specimen to the crossing electron probe and is proportional to the imaginary part of the energy-loss function, $Im(-1/\varepsilon)$

$$S(E) = (2I_ot/\pi a_om_ov^2)\, Im(-1/\varepsilon(E))\, \ln[1+(\beta/\theta_e)^2] \quad (1)$$

where I_o is the zero-loss intensity, t is the specimen thickness, v is the speed of the incident electron, a_o is the Bohr radius, m_o is the electron rest mass, β is the collection angle and θ_e is the characteristic scattering angle. The local properties of the complex dielectric function $\varepsilon(E) = \varepsilon_1 + i\varepsilon_2$ can be determined by the Kramers–Kronig transformation [11]. The imaginary part of dielectric function $\varepsilon_2(E)$ and the SSD can be related to be proportional to the product of $M^2\rho$ [11]. Bruley and Brown [12] have shown that for parabolic bands the joint DOS is

$$\rho(E) \propto (E - E_g)^{0.5} \quad (2)$$

For the direct bandgap case, the matrix element acts as a multiplicative constant to the joint DOS $\rho(E)$ and SSD is proportional to an $(E - E_g)^{0.5}$ term, while the matrix element for indirect transitions are shown to be dependent on the momentum transferred by the incident fast electron to the crystal electrons. The product of the indirect matrix element and joint DOS gives an $(E - E_g)^{1.5}$ term contributing to the SSD [3]. The SSD region near the bandgap can then be fitted using the expression $a(E - E_g)^c$, where E_g is the energy of bandgap, a is simply a pre-factor, c is about 0.5 for direct bandgap and about 1.5 for indirect bandgap [3].

The EELS analyses of dielectric function and bandgap properties in GaN and related materials (InGaN and AlN, etc.) were usually performed with a cold field-emission gun (FEG) in the scanning transmission electron microscope (STEM) (focus probe) mode [3–10,13,14]. Since a cold FEG-STEM has a typical energy resolution near 0.35 eV and the probe size can be near 0.3 nm, it allows the bandgap of >2 eV to be extracted with a spatial resolution on the scale of a few nanometres. Batson *et al.* pioneered the detection of local variations in the bandgap using a purpose-modified VG STEM on GaAs/InGaAs structures [13]. The concept of 'bandgap mapping' was proposed to map the inhomogeneity of band energy in the III–V semiconductor with a spatial resolution of a few nanometres in the STEM with the focus beam mode [14]. The spatial resolution for the bandgap analysis at an energy loss of ~3–4 eV is usually limited by the delocalization to ~7–10 nm for a fine electron probe [11,15]. To obtain the bandgap map, basically, two-dimensional spectra in *x*–*y* space have to be recorded and analysed. However, the focused beam may produce damage in the GaN and related materials [16]. The excitation effect may

also complicate the interpretation of the EELS spectrum in which case the Slater transition and core-hole effect may have to be considered [4]. The use of electron spectroscopic imaging (ESI) in an energy-filtered transmission electron microscope (EFTEM) has attracted much attention, because of the ability to directly observe the image and quantitatively analyse two-dimensional EELS spectra. The ESI has the advantage in recording two-dimensional EELS spectra from a large area with less damage in the materials, since it introduces a relatively parallel beam [17–21]. However, every image needs at least 3 s in the low-loss regime for the ESI method as the electron beam is expanded. The low-loss spectrum needs only a subsecond in the focus beam mode due to the high density of the electrons. As for application of ESI, two-dimensional quantitative elemental maps [22,23] and sp^2/sp^3 ratio maps [20] can be obtained utilizing the core-loss signal, while a dielectric function map can be deduced from the low-loss regime [21]. A set of signal processing techniques, such as fast Fourier transform (FFT) interpolation, wavelet transformation and maximum entropy deconvolution, etc., were employed to help extract the information of the dielectric function and sp^2/sp^3 ratio maps from the low-loss and core-loss ESI spectra, respectively [20,21]. In this paper, we extend our previous method to fulfil the proposal of the 'bandgap energy map' suggested by Bangert *et al.* using the ESI technique [14].

The essential challenge on analysing the bandgap region is to separate the bandgap signal from the fading tail of the zero-loss peak (ZLP) and from the noise. It may require higher energy resolution and higher energy dispersion than required for the analysis of the dielectric function in this low-loss range. Several possibilities have been reported to remove the ZLP in order to extract the data resulting from bandgap interaction: subtracting a scaled pure ZLP [22], subtracting a simulated ZLP [6,14] and deconvoluting the recorded spectrum with a modelled or experimentally acquired ZLP from the vacuum using a Fourier-ratio method [11]. Previous work [9,10] had great success in extracting the bandgap energy of GaN and related materials by applying the Fourier-ratio method to remove the ZLP and following that by convolving the spectrum with a suitable Gaussian peak, typically with a width in the range of the energy resolution, to avoid the domination of high-frequency artefacts. Although the deconvolution of the ZLP from the raw data is particularly critical when attempting to study the near bandgap region of materials with a bandgap <1.5 eV [23], it has been shown that it is possible to extrapolate bandgap energy by fitting $a(E - E_b)^c$ from the single scattered data in the first 1.5 eV region and obtain useful information from the calculated $M^2\rho$ product [23].

In this paper, we do not attempt to push the energy resolution of reconstructed ESI spectra to extract the bandgap energy near 1.5 eV or less, but, instead, try just a demonstration that a two-dimensional energy bandgap map can be possibly reconstructed from ESI series images. From the bandgap map, inhomogeneity in the quantum-well

structure can be revealed. We have chosen multilayer GaN/AlN for this study. There are three reasons for selecting these materials. First of all, GaN and AlN are both direct band materials and their band energies have been determined using EELS to be ~3.4 and 6.1 eV [10], respectively, which may be extracted using the ESI technique in a Schottky emission TEM that is usually associated with a lower dispersion (usually 1 eV) and lower energy resolution (~1 eV) than those of a cold FEG-dedicated STEM (typically, 0.1 eV dispersion and ~0.35 eV energy resolution). Second, the differentiation between 3.4 and 6.1 eV is not as difficult as the resolving of the sub-eV difference between the InGaN and GaN quantum pair. Last, it has been reported that there is no interdiffusion between GaN and AlN [24]. It makes GaN/AlN an ideal material system for an energy bandgap study, since it involves no formation of ternary alloys that may cause complication in the determination of energy bandgap.

In our work, different energy-loss images were registered by phase correlation that gives an accuracy of 1 pixel, which is equivalent to a spatial resolution of 0.5 nm calibrated from the magnification of the ESI images. The EELS spectra were extracted from a series of ESI images, followed by FFT interpolation to improve the energy dispersion. The detailed principle of the FFT interpolation can be found in our previous publications [20,21]. To avoid strong diffraction effects, the sample was tilted away from the zone axis, keeping the interface in edge-on orientation [25,26]. After Fourier-ratio deconvolution, the SSD spectra were fitted with the equation $a(E - E_g)^c$ to extract the information on bandgap energy. A multivariable least square algorithm (MVLS) is derived and given in this paper to refine the value of the energy bandgap. A threshold filter method to estimate the average value and SD of the band energy from the band-energy map of barrier and well regions is proposed.

Experimental

The GaN/AlN multilayer structure was grown by molecular beam epitaxy on an AlN buffer layer of several micrometres at a temperature of 700–750°C. The averaged thicknesses of GaN and AlN mutilayers are near 5–10 nm. Both AlN and GaN have wurtzite structure. The lattice parameters are $a = 3.110$ Å, $c = 4.980$ Å, $\alpha = \beta = 120°$ and $\gamma = 90°$ for AlN, and $a = 3.189$ Å and $c = 5.185$ Å for GaN. The TEM samples were prepared using regular mechanical polishing and ion-milling techniques. This study was performed on a JEOL 2010F TEM operated at 200 kV that was equipped with a Schottky-type emission gun and a Gatan imaging filter (GIF). The ESI series were recorded on a Gatan 1024 × 1024 slow-scan charge-coupled device camera. In the FEG-TEM presented here, the energy spread of the electron beam was optimized to ~1 eV for ESI. The width of the energy-selecting slit was set to 1 eV. The exposure time of each image is 3 s. The collection semi-angle, β, is 10 mrad. An image series consisting of 75 ESI images was recorded from −4 to 70 eV loss with a step of 1 eV. In this research, we have

employed a phase correlation technique to align the ESI images with an accuracy of 1 pixel. The pixel resolution in our experimental ESI series is 0.5 nm pixel^{-1}, calibrated from the magnification. To avoid complication from isochromaticity of the GIF in the energy-loss images, only the central 256 × 256 pixels of the images were used for the band-energy analysis. The ESI spectra were extracted and FFT-interpolated with the method that has been described in detail elsewhere [20,21]. The ESI spectra were then deconvoluted with a zero-loss ESI spectrum extracted from the vacuum region, before they were fitted with the DOS function. An iterative MVLS algorithm was developed for refining the analytical form DOS function $a(E - E_g)^{0.5}$. In the following section, the principles of the phase correlation technique and the iterative algorithm are discussed. The principles of the reconstruction of ESI spectra can be found in our previous publications [20,21].

Methodology

Phase correlation method

It is known that the registration between two images can be determined from cross correlation of these two images [27]. The cross-correlation function (CCF) $C(x, y)$ is defined as

$$C(x,y) = \mathbf{F}^{-1}[\mathbf{F}(I_1)\mathbf{F}(I_2)^*\} \tag{3}$$

where $\mathbf{F}$ and $\mathbf{F}^{-1}$ are the Fourier and inverse-Fourier operator, respectively, and I_1 and I_2 are the two images. $\mathbf{F}(I_2)^*$ denotes the conjugate of the Fourier transform of I_2. Ideally, the peak value of the correlation surface $C(x, y)$ should be equal to 1.0. However, in reality, due to the presence of random noise, the peak value will be less than 1.0. Therefore, the translation values are estimated by the maximum value in $C(x, y)$. In fact, only the phase part of $\mathbf{F}[C(x, y)]$ contains the information of the relative shift of two images. A phase correlation function (PCF) $P(x, y)$ was proposed by setting all Fourier moduli of the product $\mathbf{F}(I_1)\mathbf{F}(I_2)^*$ to be 1 [28]. The $P(x, y)$ is formulated as follows

$$P(x,y) = \mathbf{F}^{-1}[\mathbf{F}(I_1)\mathbf{F}(I_2)^*/|\mathbf{F}(I_1)\mathbf{F}(I_2)^*|] \tag{4}$$

The main difference between the PCF and regular CCF is that the PCF usually gives a much sharper peak, close to a 1 pixel delta-function, which shows the precise relative shift between two images, while the $C(x, y)$ usually displays as a broad and smooth peak that may be smeared out in the case of high noise/signal images. Figures 1a and 1b show two test images that have a relative shift, and Figs 1c and 1d show the $C(x, y)$ and $P(x, y)$, which illustrate the basic difference between them. The $P(x, y)$ shows a delta-peak which allows us to register different energy-loss images with an accuracy of 1 pixel.

Iterative MVLS fit

As mentioned earlier, for band-energy analysis the SSD is needed to fit to the analytical form of the DOS function $a(E - E_g)^{0.5}$ near the energy bandgap. The SSD can be
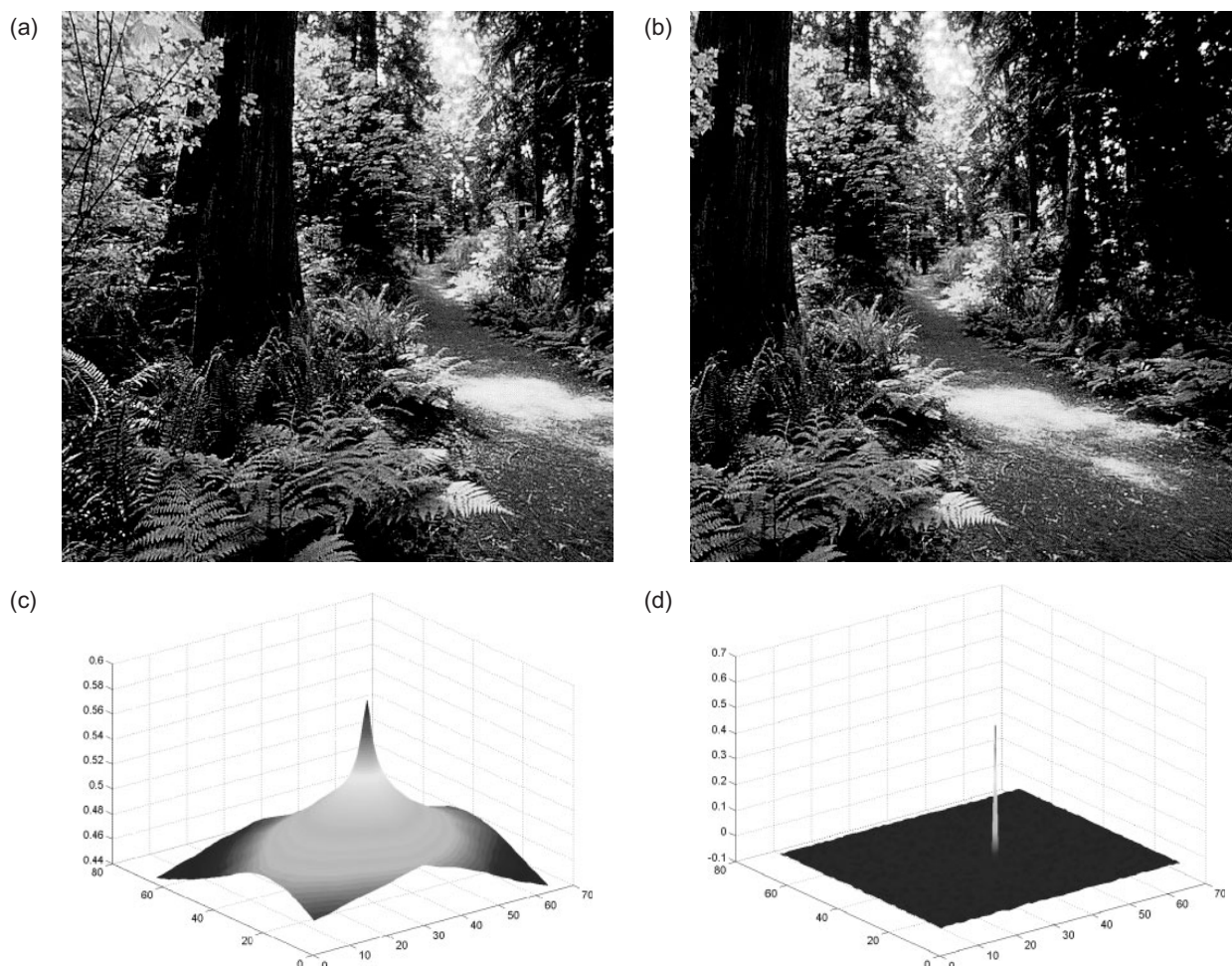
(a)

(b)

(c)

(d)

Fig. 1 (a, b) Two test images that are shifted relatively. (c, d) The CCF and PCF, respectively.

deduced by deconvoluting ESI spectra from the ZLP extracted from the vacuum by the Fourier-ratio method. There are two parameters that need to be optimized: the pre-factor 'a' and the bandgap energy E_g in $a(E - E_g)^{0.5}$. An iterative MVLS algorithm is derived here for fitting SSD to this function. Let us define a function f to be the difference between the $a(E - E_g)^{0.5}$ denoted as I^{model} and the SSD near the bandgap energy denoted as I^{ssd}

$$f = a(E - E_g)^{0.5} - I^{ssd} = I^{model} - I^{ssd} \quad (5)$$

and

$$\chi^2 = \sum (a(E_i - E_g)^{0.5} - I_i^{ssd})^2 = \sum f_i^2 \quad (6)$$

where χ^2 is a figure of merit between the model and the SSD. χ^2 is a sum over the data 5 eV above the bandgap energy of the corresponding materials in our present study. The initial values of a_o and E_{go} can be obtained from eqs (3–4) and (3–5) of [29]. The next optimum solution of 'a' and E_g can be obtained by

$$a = a_o + da \quad (7a)$$

$$E_g = E_{go} + dE_g \quad (7b)$$

where da and dE_g are the small changes in pre-factor 'a' and band energy E_g that are given follows

$$\begin{bmatrix} da \\ dE_g \end{bmatrix} = \begin{bmatrix} F_a^2 & F_a F_{E_g} \\ F_{E_g} F_a & F_{E_g}^2 \end{bmatrix}^{-1} \begin{bmatrix} F_o F_a \\ F_o F_{E_g} \end{bmatrix} \quad (8)$$

where F_a, F_{E_g} are the derivatives with respect to 'a' and E_g. The F_o is the function of f evaluated at the current values of a_o and E_{go}. The optimum solution of 'a' and E_g can be obtained usually by several tens of iterations.

Results and discussion

The experimental ESI series is shown in Fig. 2a. The thicknesses of multilayered GaN (two dark layers)/AlN (bright layer between GaN) are ~5–10 nm. A high-resolution TEM (HRTEM) image of a local area of the GaN/AlN multilayer structure is shown in Fig. 2b. Non-uniformity in the wells can be seen from the variation of contrast in Figs 2a and 2b. The EELS spectra near the Al L-edge acquired using a nano-beam from the middle of the AlN layer (marked A) and the GaN layer (marked B) are shown in Fig. 2c. Although it is suggested that no interdiffusion and reaction occurs between AlN and GaN under our processing
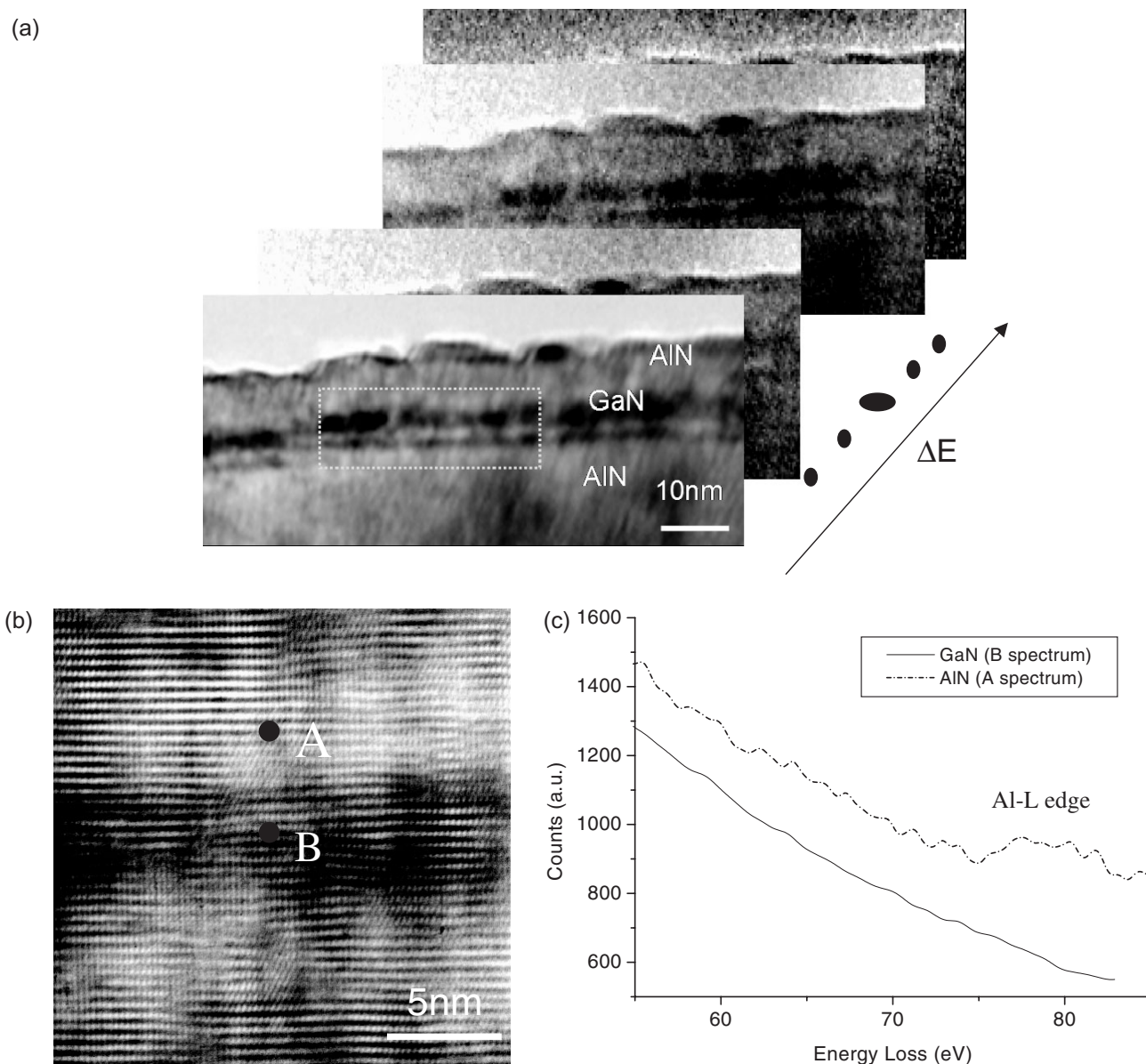
(a)

(b)

(c)

Fig. 2 (a) ESI series images of GaN/AlN layer structure. (b) HRTEM view of a local area of GaN/AlN multilayer structure. (c) The nano-beam EELS spectra from the centre of the AlN and GaN layers, marked A and B in (b), respectively.

condition [24] and the signal of Al in GaN is not obvious in EELS spectrum, we may not avoid the presence of Al in the GaN layer due to the detection limit. The ESI spectra can be extracted from ESI series images by averaging the intensity of several neighbour pixels, which depends on the pixel resolution and the spatial resolution of the ESI series. The pixel resolution in Fig. 2a is 0.5 nm pixel^{-1}. The extracted spectra are averaged from a square of 3×3 pixels, which is equivalent to an area of 1.5×1.5 nm^2. Comparison of the probe-acquired spectra (solid line) with equivalent beam size and typical extracted ESI spectra (circled line) from the AlN and GaN layers is given in Figs 3a and 3b, respectively. As reported previously [3,9], the GaN has two characteristic peaks near 19.2 and 23.3 eV, and the plasma peak of AlN is at 21 eV. The major peak around 19.4 eV is reported to result

from transition of Ga 3d electrons and has been observed in synchrotron ellipsometry and electron spectroscopy [8,30]. This double peak was not observed in the case of AlN. The peak positions of both GaN and AlN are consistent with those observed by Brockt and Lakner [10]. No dislocations were observed in our selected region; for this reason, the effect of defects was not conferred.

The ESI spectra can be FFT interpolated to improve the dispersion, as given in our previous publications for the low-loss region and carbon K-edge [20,21]. It is worth mentioning that FFT interpolation has to be used with caution: the intensity in the low-loss regime is strong so that the noise usually may not cause much problem in the low-loss regime for FFT interpolation; however, noise is a problem for FFT interpolation in the core-loss regime due to low signal. In the
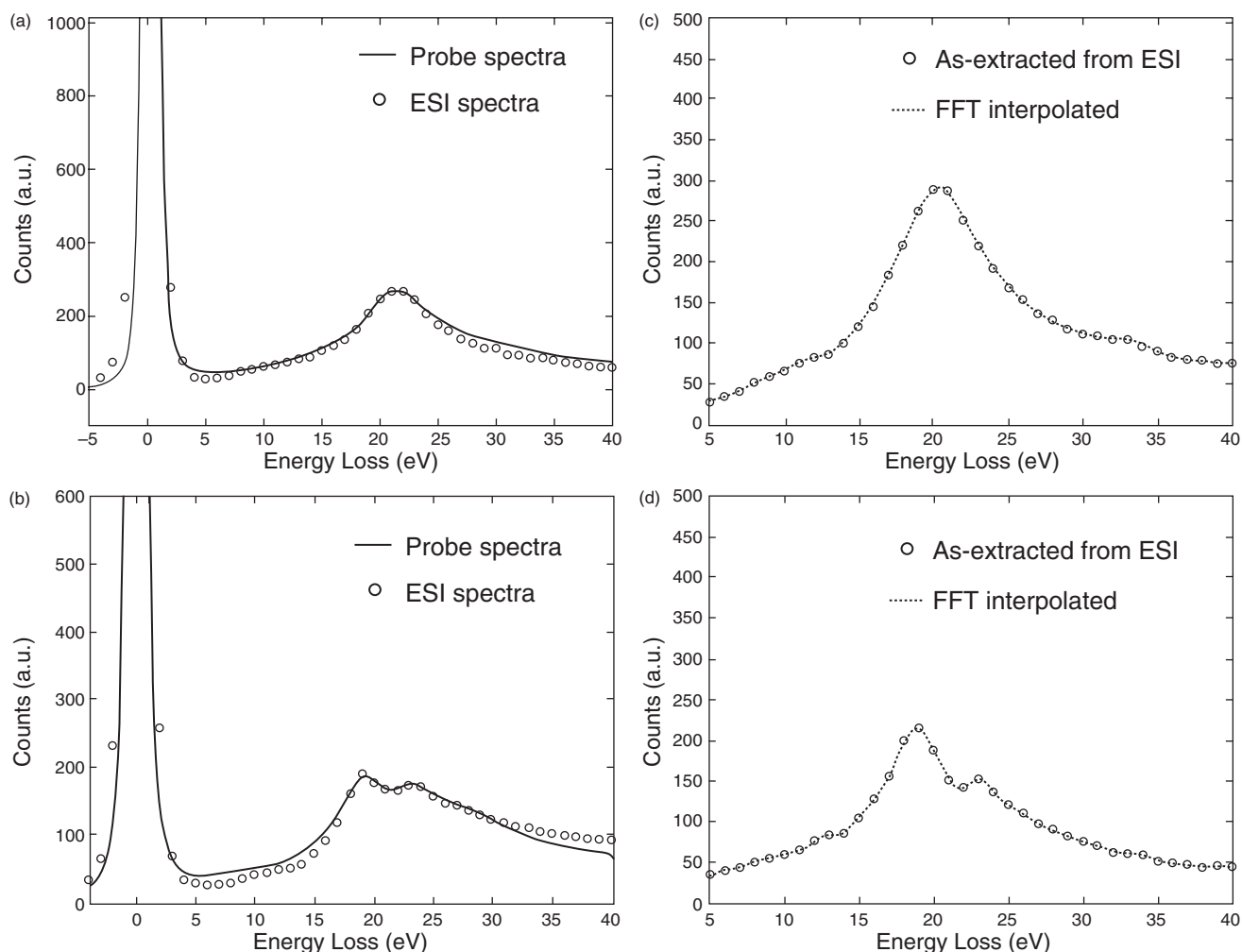
Fig. 3 Comparison of the probe-acquired low-loss spectra (line) and the as-extracted ESI spectra (circles) from (a) AlN and (b) GaN layers, respectively. (c, d) Examples of the FFT-interpolated spectra for AlN and GaN, respectively. The circles in (c) and (d) are the as-extracted data from ESI images and the lines are the FFT-interpolated data.

core-loss regime, a wavelet denoise method has to be applied before the FFT interpolation [21]. Furthermore, as mentioned previously [20,21], FFT interpretation may cause artefacts in the two ends of the data, but this problem can be solved by a flip-over method proposed in our previous publication [21]. The detailed principles of FFT interpolation also can be found in our previous publications [20,21]. The original sampling step of the extracted ESI spectra was 1 eV and that was interpolated to be near 0.12 eV, as in the case of the optical dielectric function in our previous publication [21]. Figures 3c and 3d show examples of FFT-interpolated spectra for AlN and GaN, respectively. The circled lines in Figs 3c and 3d are the as-extracted data from ESI images and the dotted lines are the FFT-interpolated data. As we can see, the FFT-interpolated data closely follow the same trend as the as-extracted data. Before band-energy analysis, SSD associated with both extracted and FFT-interpolated ESI spectra can be deduced by Fourier-ratio deconvolution with a zero-loss peak extracted from the vacuum in the hole of

the sample, as proposed previously [9–11]. The complete procedure for analysing the energy bandgap map is given in Fig. 4.

The boxed area from the zero-loss image in Fig. 2a was used for band-energy analysis. The size of the image is 200×40 pixels. Although it is suggested that the analytical form of the DOS function is only suitable within 3 eV above the band energy [3], the SSDs of AlN and GaN seem to increase monotonically from their corresponding band energies of 6.1 and 3.4 eV up to energy losses of 14 and 12 eV for AlN and GaN, respectively. Two energy ranges, 3–8 and 6–11 eV, are used for the band-energy analysis, corresponding to 5 eV above the band energy for GaN and AlN, respectively. The initial value of a_o and E_{go} of SSD from every pixel can be first estimated [29] for the two energy ranges. The value of χ^2 in eq. (6) was then calculated for each energy range. The initial values of a_o and E_{go} associated with the minimum χ^2 are assigned to the corresponding pixel to form two maps of pre-factor and band energy. These maps are used as inputs for
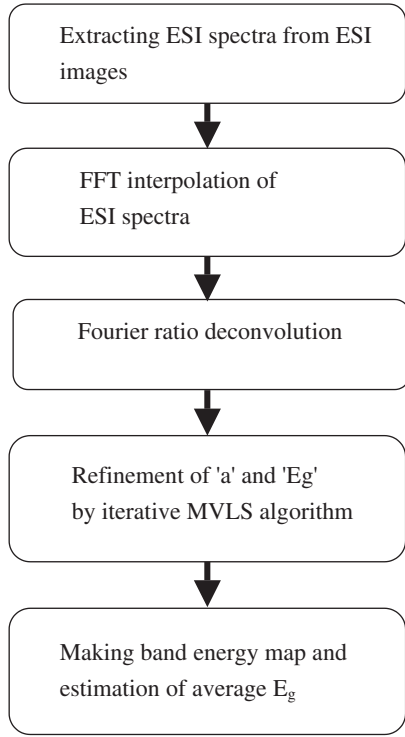
Fig. 4 A flow chart of procedures for mapping and analysis of bandgap energy.

further refining process by the iterative MVLS algorithm. The typical results of fitting the SSD to the DOS function $a(E - E_g)^{0.5}$ for AlN and GaN are depicted in Figs 5a and 5b, respectively. The circles are the SSD and the solid lines are the fitted DOS function deduced from the optimum fitting values of parameters of pre-factor 'a' and band energy E_g.

The map of bandgap energy from the boxed area in Fig. 2a is shown in a three-dimensional colour surface view in Fig. 6a. A band-energy profile (along the x-axis) across the barrier/well from Fig. 6a is depicted in Fig. 6b. Regions of the energy barrier and the well can be distinguished clearly in Fig. 6b, but inhomogeneity in the band energy also can be seen from Fig. 6a. A simple thresholding procedure was used to decide which area corresponded to AlN and which to GaN, and the average band-energy of each area was then calculated. A binary image where the barrier (or well) region is 1 and well (or barrier) region is 0 can be created by assigning proper threshold band-energy, so that 0 or 1 is assigned to the pixel whose band energy is lower or higher than this threshold energy. If the map of band energy (Fig. 6a) and the binary image are denoted as I_{Eg} and I_b, respectively, then the average band-energy can be formulated as follows

$$E_{av} = \Sigma(I_{E_g} \times I_b)/\Sigma I_b \qquad (9)$$

The SD of band energy σ_{Eg} can be evaluated using the following equation

$$\sigma_{E_g} = \left(\sum (I_{E_g} - E_{av})^2 \Big/ \sum I_b \right)^{1/2} \qquad (10)$$

The number of pixels in the corresponding AlN (barrier) and GaN (well) regions are determined from the binary images
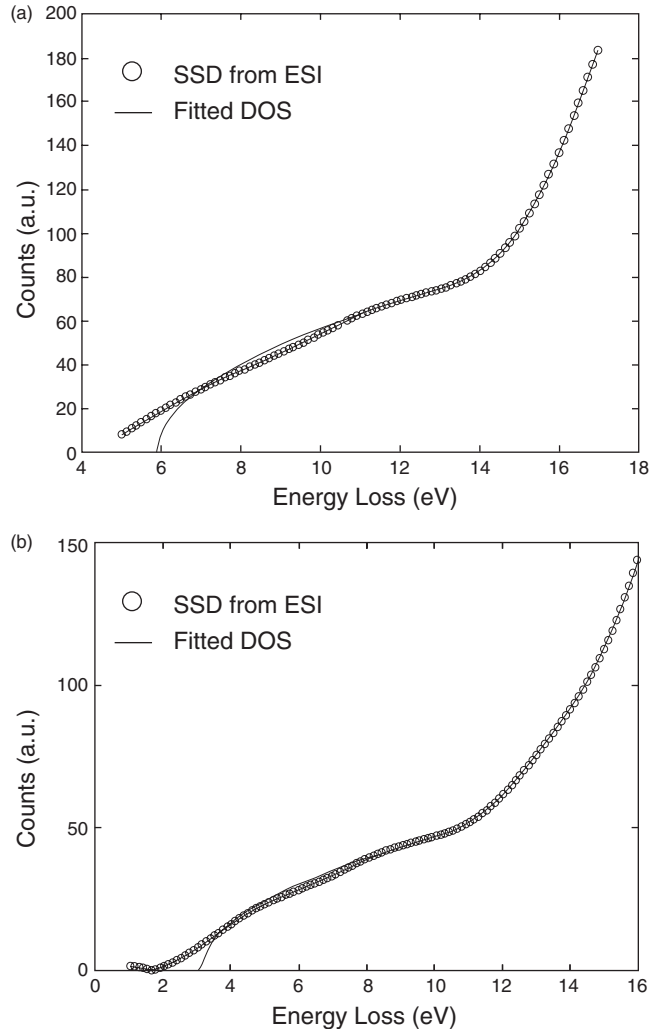

Fig. 5 (a, b) Typical results of fitting the SSD to the analytical DOS function $a(E - E_g)^{0.5}$ for AlN and GaN, respectively. The circles are the SSD and the solid curves are the fitted DOS function deduced from the optimum fitting values of parameters of pre-factor 'a' and band energy E_g.

I_b ($= \Sigma I_b$) to be 6120 and 1880 pixels, respectively. The bandgap energy of AlN and GaN is determined to be 5.62 ± 0.35 and 3.87 ± 0.36 eV, respectively, from the boxed area of Fig. 2a.

The accuracy in the band-energy analysis strongly depends on delocalization, the energy resolution of the electron source and recording method. A crude estimate of the delocalization length for a typical plasmon (low) loss is ∼5 nm [15], which is comparable to the thickness of the quantum well here. Therefore, an ESI spectrum may contribute from neighbouring pixels extended to 5 nm; however, it will be weighted by a function called the inelastic decay function [15] that describes the weighted decay contribution of the inelastic signal as a function of the distance away from the position of extracting pixel. The inelastic decay function is a function of the delocalization distance and the loss energy. Egerton [31] gave a more realistic
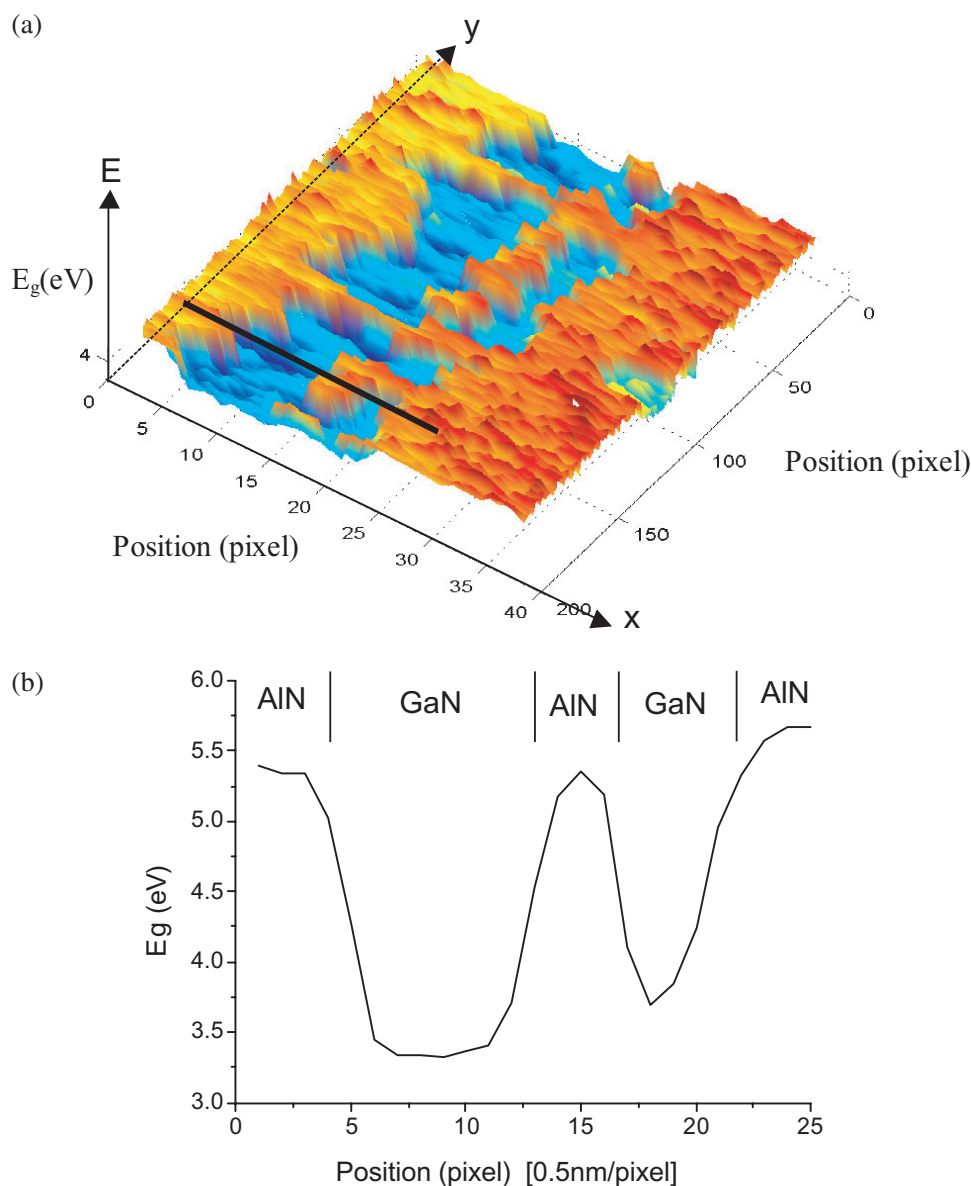
Fig. 6 (a) Map of band energy in a three-dimensional colour surface view. (b) Band-energy profile (along the *x*-axis) across the barrier/well.

estimate of delocalization diameter d_{50} (containing 50% of the scattered electrons) that approximates $0.8\lambda(E_o/E)^{3/4}$. For an incident electron of energy E_o = 200 keV, λ = 0.251 nm and energy loss E = 5 eV, the d_{50} is ∼5 nm. This implies that if an energy-loss spectrum is recorded using a highly focused probe, half of the signal will come from an area of 5 nm in diameter. The delocalization effect may explain the reason why our average band-energy for GaN is higher than the ideal value, while that of AlN is lower than its typical energy, since we expect the GaN ESI spectrum may be mixed with the inelastic signal from the AlN region and vice versa. It might be possible to improve the accuracy of the band energy, distorted by delocalization, by a signal-processing method, but it requires knowledge of the inelastic decay function, which is out of the scope of this paper.

However, it is an interesting and desired research work in the future.

The second factor affecting the accuracy of the band-energy determination is the energy spread of the electron source. Most of the previous work [3–14] in band-energy analysis for GaN and related materials has used a cold FEG. In that case, a band energy of ∼3 eV can be revealed easily, directly in some cases or without much effort in analysis. In our experiment, a Schottky-type emission TEM was used, the energy resolution is optimized to be ∼1 eV, and ESI spectra were recovered with 1 eV energy slit and 1 eV energy sampling. Although the FFT interpolation may help in energy dispersion, the energy resolution is still limited to be at best 1 eV. The accuracy in band-energy analysis in the ESI case is reasonably estimated to be about half of the energy

resolution, which has about the same magnitude as $2\sigma_{E_g}$. The ESI technique at this moment might not be able to resolve a small difference in the band energy of the barrier/well pair, as in the InGaN/GaN system, where the value is 0.5 eV. It is found that great care has to be taken in applying ESI to reveal a reliable band-energy as small as 3 eV. The energy resolution of ESI may depend not only on the electron source but also on the allowed energy width and sampling step in energy space. The smallest allowable energy width and energy sampling interval for the present GIF2000 is 1 eV. Development of a high brightness monochromatic TEM and GIF with an energy slit width and energy sampling interval as small as the energy resolution of the monochromatic TEM may allow for ESI to obtain a larger area of two-dimensional information on small band-energy and even the electronic structure from the EELS fine structure.

Concluding remarks

The concept of 'bandgap mapping' was proposed by Bangert *et al.* [6] to map the inhomogeneity of band energy in III–V semiconductors with a spatial resolution of a few nanometres in a STEM with the focus beam mode. In this paper, the map of band energy of AlN/GaN layers is obtained using the ESI technique. A threshold filter method is proposed to estimate the average value and SD of band energy from barrier and well regions in the band-energy map. The average bandgap energy of AlN and GaN is determined to be about 5.62 ± 0.35 and 3.47 ± 0.36 eV, respectively. It is thought that the delocalization effect is one of the main sources that contribute to deviation of the band energy from their ideal values. The $2\sigma_{E_g}$ accuracy of this result is comparable to half of the energy resolution of the ESI experiment.

Acknowledgements

References

1 Gil B (1998) *Group III Nitride Semiconductor Compounds*. (Clarendon Press, Oxford.)

2 Nakamura S and Chichibu S F (2000) *Introduction to Nitride Semiconductor Blue Lasers and Light Emitting Diodes*. (Taylor and Francis, London.)

3 Rafferty B and Brown L-M (1998) Direct and indirect transitions in the region of the band gap using electron-energy-loss spectroscopy. *Phys. Rev. B* **58:** 10 326–10 337.

4 Keast V J, Scott A J, Kappers M J, Foxon C T, and Humphreys C J (2002) Electronic structure of GaN and $In_xGa_{1-x}N$ measured with electron energy-loss spectroscopy. *Phys. Rev. B* **66:** 125 319–7.

5 Keast V J, Kappers M J, and Humphreys C J (2003) Electron energy-loss near edge structure (ELNES) of InGaN quantum wells. *J. Microsc.* **210:** 89–93.

6 Bangert U, Harvey A J, Freundt D, and Keyse R (1997) Highly spatially resolved electron energy-loss spectroscopy in the bandgap regime of GaN. *J. Microsc.* **188:** 237–242.

7 Gutierrez-Sosa A, Bangert U, Harvey A J, Fall C, and Jones R (2003) Energy loss spectroscopy of dislocation in GaN and diamond: a comparison of experiment and calculations. *Diamond Rel. Mat.* **12:** 1108–1112.

8 Olson C G and Lynch D W (1981) 10–30-eV optical properties of GaN. *Phys. Rev. B* **24:** 4629–4633.

9 Lakner H, Rafferty B, and Brockt G (1999) Electronic structure analysis of (In, Ga, Al)N heterostructures on the nanometer scale using EELS. *J. Microsc.* **194:** 79–83.

10 Brockt G and Lakner H (2000) Nanoscale EELS analysis of dielectric function and bandgap properties in GaN and related materials. *Micron* **31:** 435–440.

11 Egerton R F (1996) *Electron Energy-Loss Spectroscopy in Electron Microscopy*. (Plenum, New York.)

12 Bruley J and Brown L M (1987) *Analytical Electron Microscopy Workshop, Proceedings,* ed. Lorimer G W. (Institute of Metals, London, 1988.)

13 Batson P E, Kavanagh K L, Woodall J M, and Mayer J W (1986) Electron-energy-loss scattering near a single misfit dislocation at the GaAs/GaInAs interface. *Phys. Rev. Lett.* **24:** 2729–2732.

14 Bangert U, Harvey A J, and Keyse R (1997) Assessment of electron energy-loss spectroscopy below 5 eV in semiconductor materials in a VG STEM. *Ultramicroscopy* **68:** 173–180.

15 Muller D A and Silcox J (1995) Delocalization in inelastic scattering. *Ultramicroscopy* **59:** 195–213.

16 Sun H P, Li H, Li H D, Zou G T, Zhang Z, and Pan X Q (2001) Electron beam irradiation induced structural modulation and damage in GaN nano crystals. *Microsc. Microanal.* **7** [Suppl. 2]: 492–493.

17 Martin J, Plitzko J M, Spolenak R, Keller R-M, and Meyer J (1999) Quantitative electron spectroscopic imaging studies of microelectronic metallization layers. *J. Microsc.* **194:** 71–78.

18 Liu C P, Boothroyd C B, and Humphrey C J (1999) Energy-filtered transmission electron microscopy of multilayers in semiconductors. *J. Microsc.* **194:** 58–70.

19 Botton G A and Phaneuf M W (1999) Imaging, spectroscopy and spectroscopic imaging with an energy filtered field emission TEM. *Micron* **30:** 109–119.

20 Yang J-Y, Chen F-R, and Kai J-J (2002) Mapping of sp2/sp3 in DLC thin film by signal processed ESI series energy-loss image. *J. Electron Microsc.* **51:** 391–400.

21 Lo S-C, Kai J-J, Chen F-R, Chen L-C, Chang L, Chang C-C, Ding P-J, Chin B, Zhang H, and Chen F-S (2002) Four-dimensional dielectric property image obtain from electron spectroscopic imaging series. *J. Electron Microsc.* **50:** 497–507.

22 Rafferty B E (1997) *Probing Electronic Structure near the Bandgap Region using Electron Energy Loss Spectroscopy*. (Thesis, University of Cambridge, UK.)

23 Alexandrou I, Papworth A J, Rafferty B, Amaratunga G A J, Kiely C J, and Brown L M (2001) Calculation of the electronic structure of carbon films using electron energy loss spectroscopy. *Ultramicroscopy* **90:** 39–45.

24 Khan M, Kuznia J, Olson D, George T, and Pike W (1993) GaN/AlN digital alloy short-period superlattices by switched atomic layer metalorganic chemical vapor deposition. *Appl. Phys. Lett.* **63:** 3470–3472.

25 Schenner M, Nelhiebel M, and Schattschneider P (1996) Diffraction effects in electron spectroscopic imaging. *Ultramicroscopy* **65:** 95–99.

26 Moore K T, Howe J M, and Elbert D C (1999) Analysis of diffraction contrast as a function of energy loss in energy-filtered transmission electron microscope imaging. *Ultramicroscopy* **80:** 203–219.

27 Gonzalez R C and Woods R E (1992) *Digital Image Processing*, p. 109. (Addison-Wesley, Reading Massachusetts.)

28 Kuglin C D and Hines D C (1975) The phase correlation image alignment method. In: *Proceedings of the IEEE International Conference on Cybernetics and Society*, pp. 163–165.

29 Rabinowicz E (1969) *An Introduction to Experimentation*, pp. 72–73. (Addison-Wesley, Reading, MA.)

30 Hedman J and Martensson N (1980) Gallium nitride studied by electron spectroscopy. *Phys. Scripta* **22:** 176–178.

31 Egerton R F (2003) New techniques in electron energy-loss spectroscopy and energy-filtered imaging. *Micron* **34:** 127–139.